OPTICS

A quantum-enhanced wide-field phase imager

Robin Camphausen[1]*, Álvaro Cuevas[1]*, Luc Duempelmann[1], Roland A. Terborg[1], Ewelina Wajs[1], Simone Tisa[2], Alessandro Ruggeri[2], Iris Cusini[3], Fabian Steinlechner[4,5], Valerio Pruneri[1,6]*

Quantum techniques can be used to enhance the signal-to-noise ratio in optical imaging. Leveraging the latest advances in single-photon avalanche diode array cameras and multiphoton detection techniques, here, we introduce a supersensitive phase imager, which uses space-polarization hyperentanglement to operate over a large field of view without the need of scanning operation. We show quantum-enhanced imaging of birefringent and nonbirefringent phase samples over large areas, with sensitivity improvements over equivalent classical measurements carried out with equal number of photons. The potential applicability is demonstrated by imaging a biomedical protein microarray sample. Our technology is inherently scalable to high-resolution images and represents an essential step toward practical quantum-enhanced imaging.

INTRODUCTION

Entanglement can enhance precision measurements beyond the possibilities of classical optics (1, 2). This is of particular importance to applications that necessarily involve low-photon flux, where shot noise becomes a limiting factor. Such a situation may be encountered when imaging organic or living samples that can suffer from photosensitive effects (3), including chemical changes at the molecular level or disruption of cell functions (4, 5). In the biomedical field, label-free analysis involving classical illumination is usually considered a noninvasive approach. However, recent evidence shows that, for some applications, even relatively low classical light levels suffice to induce changes in the sample, ranging from permanent photodamage (6) to more subtle alterations that, nonetheless, affect measurement accuracy (7). Photosensitivity must also be taken into account when probing fragile quantum gas states (8) or atomic ensembles (9). In all the above cases, it therefore becomes attractive to perform phase imaging using nonclassical states of light, such as N00N states consisting of N entangled photons between two optical modes, which are well known to yield a signal-to-noise ratio (SNR) enhancement of $\sqrt{N}$ over equivalent classical measurements (1, 2, 10–13). This effect is known as supersensitivity.

Entanglement-enhanced phase imaging was demonstrated already for both birefringent (14) and nonbirefringent (15) phase samples. However, neither of these works represents true imaging platforms as the entangled photons probing a sample were detected with single-pixel detectors and images were constructed by scanning the sample point by point. This inherently limits scalability owing to a range of practical drawbacks, which can include mechanical vibrations and long-term reliability issues caused by moving parts, synchronization between pixel-scanning and light detection necessitating complex calibration procedures, and prohibitively long scanning times.

Here, we show an entanglement-enabled supersensitive phase imager operating in a wide-field configuration. By exploiting hyperentanglement, that is, simultaneous N00N state entanglement in the polarization degree of freedom and correlations in a massive pixel mode state space, our system is made scan free. This enables the retrieval of phase information with a large field of view (FoV), using a single-photon sensitive single-photon avalanche diode (SPAD) array camera and computational methods adapted from digital holography. The holographic phase retrieval method used has the advantage over conventional interferometric measurements that phases can be accurately retrieved regardless of sample absorbance and without requiring a priori knowledge of the illumination brightness and phase offset (16). Our work is made possible through recent advances in quantum imaging (17, 18) and fabrication of SPAD array cameras (19), allowing us to acquire spatially resolved multiphoton images with very high SNR. We demonstrate the experimental feasibility of our approach by retrieving precise phase images of birefringent and nonbirefringent test samples, including a protein microarray sample that demonstrates the applicability for biomedical diagnostic applications. The ability to measure birefringent phase samples has also important applications in material science and crystallography (20). We show a sensitivity enhancement over equivalent classical measurements of 1.39 ± 0.11 and 1.25 ± 0.06, for the birefringent and nonbirefringent samples, respectively. Our method is inherently scalable to larger images with more pixels and represents an essential step toward a practically useful quantum-enhanced biological and material inspection imaging platform.

RESULTS

Quantum-enhanced large FoV phase imager

Our system integrates a source of space-polarization hyperentangled N00N states, a large FoV lens-free interferometric microscope (LIM) (21), and a SPAD array camera, with computational methods for co-incidence imaging and holographic phase retrieval. As can be seen in Fig. 1A, hyperentangled photon pairs are generated by spontaneous parametric down conversion (SPDC) within a Sagnac interferometer (SI). Entanglement in the polarization degree of freedom is generated by combining the clockwise and counterclockwise photon pair generations in the SI, resulting in a two-photon N00N state $(|2_H 0_V\rangle + |0_H 2_V\rangle)/\sqrt{2}$, where H and V represent the horizontally and vertically polarized modes, respectively (22). The

[1]ICFO-Institut de Ciencies Fotoniques, The Barcelona Institute of Science and Technology, Av. Carl Friedrich Gauss, 3, 08860 Castelldefels, Barcelona, Spain. [2]Micro Photon Device SRL, Via Waltraud Gebert Deeg 3f, 39100 Bolzano, Italy. [3]Dipartimento di Elettronica, Informazione e Bioingegneria, Politecnico di Milano, Via Giuseppe Ponzio, 34, 20133 Milano, Italy. [4]Fraunhofer Institute for Applied Optics and Precision Engineering IOF, Albert-Einstein-Str. 7, 07745 Jena, Germany. [5]Abbe Center of Photonics, Friedrich Schiller University Jena, Albert-Einstein-Str. 6, 07745 Jena, Germany. [6]ICREA-Institució Catalana de Recerca i Estudis Avançats, Passeig Lluís Companys 23, 08010 Barcelona, Spain.
*Corresponding author. Email: robin.camphausen@icfo.eu (R.C.); alvaro.cuevas@icfo.eu (Á.C.); valerio.pruneri@icfo.eu (V.P.)

correlated nature of SPDC photon pair generation on the other hand yields space-momentum entanglement (*23*). As shown in Fig. 1A, the near field of the entangled state, where both photons are spatially correlated (approximately in the same spatial position) (*24*), is imaged onto a spatial light modulator (SLM), reimaged into our LIM, and detected by the SPAD array camera. After propagating through the entire setup, we express the quantum state as

$$|\Psi\rangle \approx \sum_{\mathbf{r},\mathbf{r}'}\left[|H_{\mathbf{r}}\rangle |H\rangle_{\mathbf{r}'} + e^{i2\Theta(\mathbf{r})} |V\rangle_{\mathbf{r}} |V\rangle_{\mathbf{r}'} \right] \qquad (1)$$

where we neglect normalization coefficients for clarity. Here, $\mathbf{r}$ and $\mathbf{r}'$ are the transverse coordinates of the two spatially correlated photons, which are close in space and thus acquire approximately the same phase [$\Theta(\mathbf{r}) \approx \Theta(\mathbf{r}')$]. The sample and setup therefore cause the two-photon entangled state to acquire a total phase difference between H and V of $2\Theta(\mathbf{r}) \approx \Theta(\mathbf{r}) + \Theta(\mathbf{r}')$. See Materials and Methods for details of the setup and Supplementary Materials, Section 1 (SM-S1) for the derivation of Eq. 1.

The LIM measures phase differences by interfering laterally displaced polarization states (*21*) and can be used for the inspection of large area material and biological samples such as microarrays of proteins or microorganisms for diagnostic applications (*25*). As shown in Fig. 1, the crucial components of the LIM are two Savart plates (SPs; SP_1 and SP_2). For an input beam, SP_1 laterally displaces the H-polarized photons in one direction and the V-polarized photons in the orthogonal direction, thereby introducing a shear (S) between the two polarization components. Later, SP_2 is placed with an opposite orientation to SP_1 to revert this shear, which effectively

forms a Mach-Zehnder interferometer (MZI) at each (lateral) spatial location, with the MZI modes separated from each other by the shear distance. Motorized tuning of the pitch angle of SP_1 with respect to the light propagation axis induces a controlled bias phase α between the two sheared spatial modes and associated polarization components after SP_2 (*21*, *26*), over a large scanning range $0 < \alpha < 50\pi$, with no measurable beam deviation.

In the birefringent phase imaging configuration, the total phase $\Theta(\mathbf{r})$ after SP_2 equals to $\Theta_b(\mathbf{r}) = \phi_b(\mathbf{r}) + \alpha$, where $\phi_b(\mathbf{r})$ is a spatially dependent birefringent sample phase. This is illustrated in Fig. 1B, where the shown phase profile is always between H and V polarized light. On the other hand, for measuring a nonbirefringent phase sample, the sample is placed between SP_1 and SP_2 of the LIM. In this configuration, the LIM imprints a nonbirefringent sample phase $\phi_{nb}(\mathbf{r})$ between the SPs onto a birefringent phase between H and V after SP_2. This results in the total phase $\Theta_{nb}(\mathbf{r}) = \phi_{nb}(\mathbf{r} + S/2) - \phi_{nb}(\mathbf{r} - S/2) + \alpha$, where S is the shear distance between H and V induced by the SPs, as shown in Fig. 1C.

Low-noise two-photon interference measurement using a SPAD array camera

The total phase factor $2\Theta(\mathbf{r})$ in Eq. 1 acquired by the two-photon state $|\psi\rangle$ is transformed into a measurable change in photon coincidences by projecting into the diagonal polarization bases. This is achieved by a half–wave plate (HWP) at 22.5° after SP_2, and a lateral displacement polarizing beam splitter (dPBS), which directs the photons with diagonal [$D \equiv (H + V)/\sqrt{2}$] polarization to the left half of the camera sensor and those with antidiagonal [$A \equiv (H - V)/\sqrt{2}$] polarization to the right half. Using our SPAD array camera, we

Fig. 1. Description of the experiment. (A) Scheme of the entanglement-enhanced imaging setup. SI, Sagnac interferometer; PBS, polarizing beam splitter; HWP, half–wave plate; L, lenses; P, polarizer; DM, dicroic mirror; M, mirror; ϕ_b, birefringent sample (SLM); ϕ_{nb}, nonbirefringent sample; SP, Savart plate; dPBS, lateral displacement polarizing beam splitter; BPF, band-pass filter. **(B)** Detecting birefringent phase samples with the LIM. **(C)** Detecting nonbirefringent phase samples with the LIM. In (B) and (C), three example trajectories are shown through the LIM, dashed lines correspond to H, and dotted lines correspond to V polarized light. SP_1 is tilted using the pitch angle with respect to the optical axis.

then measure spatially resolved photon coincidences (*18*) in the three possible polarization bases, corresponding to $\langle DD | \psi \rangle$, $\langle AA | \psi \rangle$, and $\langle DA | \psi \rangle$ measurements (see Materials and Methods for details). We experimentally characterized and then optimized the SNR of the measured coincidences, which depends on the entangled photon generation rate and camera acquisition parameters (see SM-S5 for details) (*27, 28*). We note that, here, a critical factor is the SPAD array camera's negligible read noise and very high frame rate, enabling the ultralow-noise acquisition of spatially resolved coincidences across 2048 spatial modes defined by the camera's pixels. The SPAD array camera is therefore an essential enabling technology for the supersensitive phase imaging presented in this work.
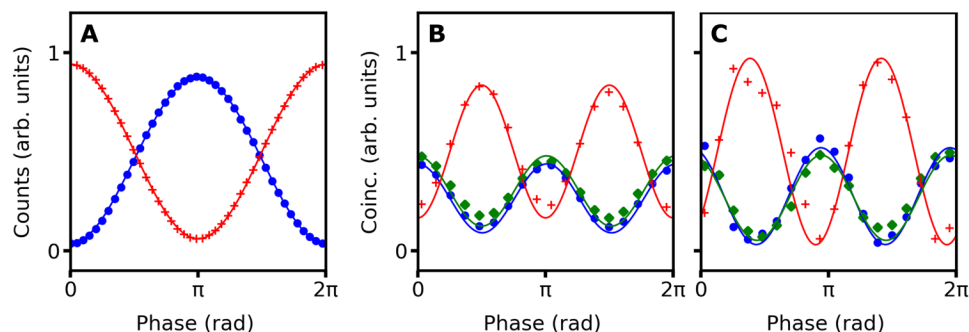
Entangled state characterization

To characterize the quality of the entangled state, we first acquired a series of coincidence count measurements (using Eq. 9 from Materials and Methods) while scanning through the LIM offset phase α, with no sample present. In Fig. 2, we see that quantum two-photon interference manifests twice the periodicity of the single-photon interference, which is the expected signature of phase superresolution for N00N state interference (*10, 12*). That is, for an offset phase α that is applied by a given tilt of SP_1 in the LIM, the classical state acquires the phase α, while the N00N state acquires the phase 2α. When integrating coincidences across the whole SPAD array camera (Fig. 2B), a relatively low fitted visibility of $\mathcal{V}_{overall} = 0.670 \pm 0.022$ is obtained. However, when analyzing the coincidences of one fixed pixel with those surrounding it (Fig. 2C), the fitted visibility is $\mathcal{V}_{local} = 0.94 \pm 0.06$. This result indicates high local fidelity with respect to the theoretical state $| \psi \rangle$, validating the supersensitive capabilities of our quantum resource (*14, 29*). The discrepancy in visibility between Fig. 2B and Fig. 2C indicates a spatially dependent phase background across the N00N state wavefront, which we characterize and remove when imaging samples (see SM-S6 for details).

Holographic phase imaging from coincidence counts

The processed coincidence counts cc_F, calculated from Eq. 9 (in Materials and Methods), represent a four-dimensional quantity (two spatial dimensions per pixel). This was transformed into a two-dimensional coincidence image (ci) using the following mapping

$$ci(x, y) = \sum_{x'=1}^{W} \sum_{y'=1}^{Z} cc_F(x, y, x', y') \qquad (2)$$

where W (Z) is the image width (height), that is, the number of pixels in the x (y) dimension of the camera sensor, and $cc_F(x, y, x', y')$ is the number of coincidences between pixels with coordinates $[x, y]$ and $[x', y']$. Equation 2 produces a two-dimensional image with the same number of pixels as the camera sensor, representing the two-photon counts at each pixel (see SM-S3 for details).
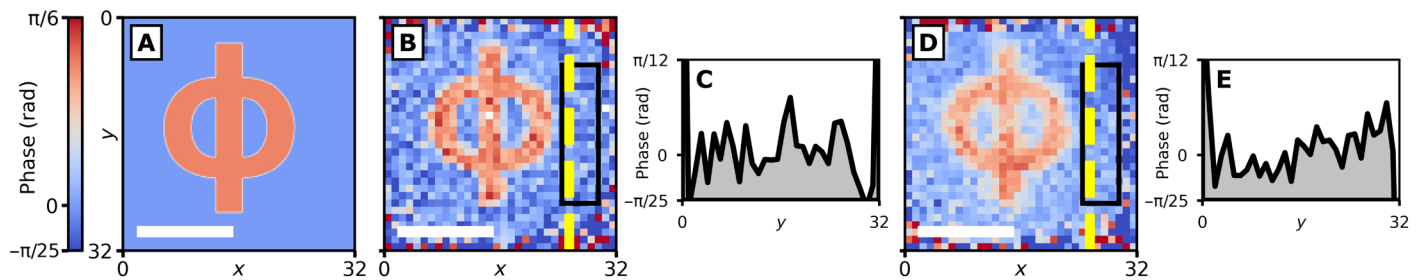
Entanglement-enhanced phase images were retrieved using phase-shifting digital holography (PSDH) (*30*), taking advantage of the tunable LIM bias phase. Coincidence images were acquired for four different bias phases α = {0, π/4, π/2, 3π/4}, where the spatially resolved coincidence image ci(**r**, α) depends on the bias α and is calculated using Eq. 2. The sample phase image is then retrieved according to

$$\hat{\phi}_{N00N}(\mathbf{r}) = \frac{1}{2} \tan^{-1} \left[\frac{ci(\mathbf{r}, \pi/4) - ci(\mathbf{r}, 3\pi/4)}{ci(\mathbf{r}, \pi/2) - ci(\mathbf{r}, 0)} \right] \qquad (3)$$

where the circumflex on $\hat{\phi}_{N00N}$ indicates that it is an estimator of the sample phase, calculated from the experimental N00N state interference. In the birefringent phase imaging configuration, Eq. 3 estimates ϕ_b, whereas, in the nonbirefringent phase imaging configuration, it estimates $\phi_{nb}(\mathbf{r} + S/2) - \phi_{nb}(\mathbf{r} - S/2)$, the sheared nonbirefringent phase. The phase image is retrieved for each of the three polarization projections ($\langle DD |$, $\langle AA |$, and $\langle DA |$) and then combined for a more accurate estimation.

Supersensitive imaging of a birefringent sample

We first investigated the entanglement-enhanced phase imaging capabilities of our system by measuring a birefringent test sample generated by the SLM (pattern shown in Fig. 3A). An equal number of photodetections was used to retrieve a phase image using classical (single-photon) intensity interference and entanglement-enhanced (two-photon) N00N state interference. Over all four phase-shifted images, a total of $I_{tot} = 8.18 \times 10^5$ single-photon detection events and $ci_{tot} = 4.06 \times 10^5$ two-photon coincidences were recorded (i.e., $I_{tot} \approx 2ci_{tot}$), in acquisition times of 2.9 s and 24 hours, respectively. Figure 3B shows the classical phase estimate image $\hat{\phi}_{Classical}$, calculated from Eq. 10 (in Materials and Methods). Figure 3D, on the other hand, shows the entanglement-enhanced phase estimate $\hat{\phi}_{N00N}$, calculated from Eq. 3. Figure 3 (C and E) shows cross sections of the background noise in the classical and entanglement-enhanced phase estimate images, respectively. Figure 3 (B and D) shows the recovered sample phase well, whose accuracy is further

Fig. 2. Classical versus N00N state interference. (**A**) Classical interference integrating across whole camera. Red crosses and blue circles correspond to $\langle D |$ and $\langle A |$ projections, respectively. (**B**) N00N state interference integrating across whole camera. (**C**) N00N state interference with a single fixed pixel. For (B) and (C), red crosses, blue circles, and green diamonds correspond to coincidence counts (Coinc.) from $\langle DA |$, $\langle DD |$, and $\langle AA |$ projections, respectively. Solid lines are fitting curves. The doubled periodicity in (B) and (C) as compared to (A) is obtained by the tilting of SP_1 in the LIM, which induces a phase α in the classical state and 2α in the N00N state.

Fig. 3. Retrieved phase images of a birefringent sample. (**A**) Phase profile applied to SLM. (**B**) Classical phase image $\hat{\phi}_{\text{Classical}}$. (**C**) Cross section of phase profile along the yellow dashed line in (B). (**D**) Entanglement-enhanced phase image $\hat{\phi}_{\text{N00N}}$. (**E**) Cross section of phase profile along the yellow dashed line in (D). Black rectangles in (B) and (D) indicate the area used for LU calculations. The pixel-to-pixel noise is reduced in (D) and (E) compared to (B) and (C). The reduced edge contrast in (D) is due to the relatively large photon spatial correlation width, but can be addressed by engineering an entangled photon source with a tighter spatial correlation. Scale bars, 1 mm at sample plane.

confirmed with the zero-normalized cross-correlation image matching metric (details in SM-S7).

To quantify the sensitivity enhancement that our protocol provides, we compute the local uncertainty (LU) of the images, that is, the root mean squared differences between all pairs of neighboring pixels (*14*). The regions indicated by the black rectangles in Fig. 3 (B and D, respectively) were used to calculate the LU, yielding $\text{LU}_{\text{Classical}} = 0.091 \pm 0.005$ and $\text{LU}_{\text{N00N}} = 0.065 \pm 0.004$, where the errors in LU represent the statistical SE. We therefore obtained a reduction in noise from $\hat{\phi}_{\text{Classical}}$ to $\hat{\phi}_{\text{N00N}}$, which can be seen qualitatively by comparing the roughness of Fig. 3 (C and E) and numerically as $\text{LU}_{\text{N00N}}/\text{LU}_{\text{Classical}} = 0.72 \pm 0.06$. The above result is consistent with the predicted phase supersensitivity for our system $\text{sd}(\hat{\phi}_{\text{N00N}})/\text{sd}(\hat{\phi}_{\text{Classical}}) = 0.79 \pm 0.05$ (see Materials and Methods or detailed calculation in SM-S5) and close to the theoretical bound of $1/\sqrt{2} \approx 0.707$.

### Supersensitive imaging of protein microarray sample

A nonbirefringent phase sample was implemented by fabricating a microarray of protein spots on a glass slide (details in Materials and Methods), similar to clinical microarray assays, where a range of capture antibodies are spotted onto a glass slide, each binding with a specific biomarker (e.g., an indicator of a disease). Measuring a change in signal for a given spot therefore confirms the presence or absence of a certain condition, aiding in rapid diagnosis (*31*). Accurately imaging the phase jumps due to the presence or absence of proteins in such a biological sample and showing a quantum enhancement in this measurement confirm the direct applicability of our entanglement-enhanced imaging system to diagnostics applications. As shown in Fig. 1C, the microarray test sample (ϕ_{nb}) was inserted into the LIM for measuring. Figure 4A shows a reference phase image retrieved under high-intensity illumination, whereas Fig. 4 (B and C) shows the low-intensity illumination (single-photon) and entanglement-enhanced phase estimates $\hat{\phi}_{\text{Classical}}$ and $\hat{\phi}_{\text{N00N}}$, respectively. As with the birefringent sample, an equal number of photodetections was used to reconstruct the phase image estimates $\hat{\phi}_{\text{Classical}}$ and $\hat{\phi}_{\text{N00N}}$ ($I_{\text{tot}} = 3.16 \times 10^6$ single-photon detection events and $\text{ci}_{\text{tot}} = 1.55 \times 10^6$ two-photon coincidences, i.e., $I_{\text{tot}} \approx 2\text{ci}_{\text{tot}}$), permitting a fair comparison of phase sensitivity for the two methods. The respective acquisition times were 3.2 s and 28 hours. Horizontal cross sections of the phase images (Fig. 4, D to F) confirm the accuracy of the entanglement-enhanced measurement compared to both classical ones. The contrast between spots and

the surrounding background, indicating the presence and absence of proteins, respectively, is clear in all measurements, which confirms the suitability of the technique for probing diagnostic microarrays. We again compare the LU, using the areas defined by the black rectangles. The extracted values are $\text{LU}_{\text{Classical}} = 0.059 \pm 0.002$ and $\text{LU}_{\text{N00N}} = 0.047 \pm 0.001$, which provides an enhancement of $\text{LU}_{\text{N00N}}/\text{LU}_{\text{Classical}} = 0.80 \pm 0.04$, again consistent with the predicted phase supersensitivity of 0.79 ± 0.05 (see Materials and Methods or detailed calculation in SM-S5) and close to the theoretical bound of $1/\sqrt{2} \approx 0.707$.

DISCUSSION

Our proof-of-principle demonstration of quantum-enhanced imaging represents a first step toward a real-world advantage for specific bioimaging use cases that require imaging sample phases with a lower photon number than classically possible. As pointed out in (*32*) and (*33*), besides photodamage, which is readily observed upon sample inspection, also experimentally important are photosensitive effects caused by illumination levels orders of magnitude below the damage threshold. Such effects may not be obvious to the user but still adversely affect measurement reliability and include altering of gene expression (*5*), enzyme activity (*7*), and acceleration of oxidation and reduction reactions in cells (*4*). Comprehensive quantitative data on these phenomena are scant (*32*), especially for phase imaging, which has only recently begun to supplant fluorescence microscopy in biomedical applications (*34*). However, for instance, in (*7*), rough calculations indicate that light-induced changes become noticeable starting from only ~10^9 to 10^{11} photons at the cell level, a light budget comparable to illumination levels enabled by state-of-the-art entangled photon sources. A promising application for quantum-enabled supersensitive imaging may then be the long-term inspection of photosensitive biosamples, such as the monitoring of biomarkers from a patient subjected to an evolving disease (*35*) or the characterization of slow changes in neural cells (*36*). In such a case, a small photon budget must be stretched across a period of hours or days, and, therefore, even the $\sqrt{2}$ sensitivity enhancement enabled by two-photon N00N states would lead to a useful improvement in measurement capacity.

Moreover, it is straightforward to extend our protocol to larger N00N states or other nonclassical light states with $N > 2$ photons. Analogously to what is shown here, if all N photons of the state are spatially correlated, a SPAD array camera can measure the $N > 2$
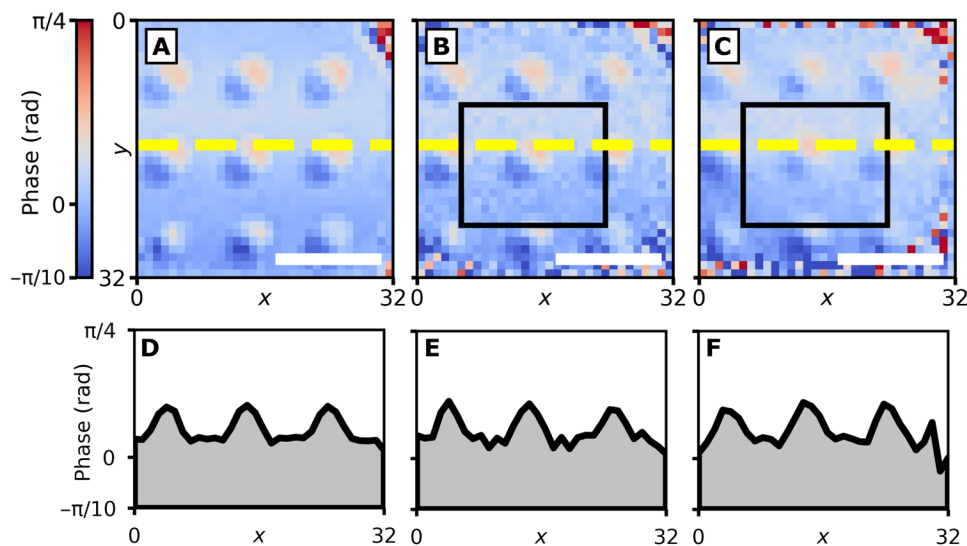
Fig. 4. Retrieved phase images of a nonbirefringent protein microarray sample. (**A**) Reference phase image from high-intensity classical illumination. (**B**) Low-intensity (single-photon level) classical illumination phase image $\hat{\phi}_{Classical}$. (**C**) Entanglement-enhanced phase image $\hat{\phi}_{N00N}$. (**D** to **F**) Cross sections of phase profiles along the yellow dashed lines in (A) to (C). Black rectangles in (B) and (C) indicate the area used for LU calculations. All three experimental conditions show clear contrast between regions of high protein binding (circular spots) to regions with no binding (background). The entanglement-enhanced method (C) manifests less pixel-to-pixel noise than its classical counterpart (B) for an equal number of photons detected. Scale bars, 2 mm at sample plane.

multiphoton coincidence images, so the phase can be retrieved using PSDH with a theoretical sensitivity enhancement of $\sqrt{N}$, rather than the $\sqrt{2}$ factor currently afforded by entangled photon pairs. However, using SPDC to generate N00N states with many photons is experimentally very challenging, with past demonstrations showing only probabilistic generation of N00N states with relatively small N (*10*, *37*). On the other hand, recent progress in quantum dot and cavity-based entangled photon sources has been promising (*38–40*), and we are therefore hopeful that N00N state sources with high N may become available in the future, which will enable greater sensitivity enhancements in our system.

In our experiment, the image resolution of 32 pixels by 32 pixels was only limited by the sensor of our SPAD array camera. On the basis of recent developments of SPAD arrays with up to megapixel resolution (*41*), we expect that our protocol can be fully exploited for highly detailed quantum-enhanced phase imaging. We note that our protocol becomes susceptible to errors when the correlation width between photons is comparable to the sample feature size, as, in this case, it is likely that the two photons acquire different phases. This implies a breakdown in the approximations that leads to Eq. 1 (details in SM-S1) and leads to reduced edge contrast, as can be seen in the blurred edges of the "ϕ" pattern in Fig. 3D. Future work will focus on developing an entangled photon source with a tighter photon pair correlation width to improve spatial resolution.

Sensitivity comparisons between the classical and quantum-enhanced measurements were made here for an equal number of photons counted, with postselection used for coincidence counting. Photon losses due to imperfect optical efficiencies were not taken into account, which is standard practice in almost all works on quantum-enhanced phase measurements to date (*10*, *11*, *14*, *15*). However, as N00N state phase measurements are highly sensitive to loss, a real sensitivity advantage can only be shown by comparing an equal number of photons at the sample (*29*), which necessitates very

high optical efficiencies (*42*). To this end, future work will focus on developing entangled photon sources at shorter wavelengths in combination with enhanced efficiency SPAD array cameras (*43*) to markedly improve system optical efficiency. Another promising approach would be to use superconducting nanowire single-photon detectors (SNSPDs), which routinely achieve detection efficiencies of close to unity (*44*). In particular, SNSPD image sensors have recently been demonstrated (*45*, *46*), which, while currently having some limitations, could, in the future, be used for the required high-efficiency coincidence image detection. Last, future work will also focus on modifying our method to achieve enhanced phase imaging using other quantum states that have less demanding optical efficiency requirements than N00N states (*47–51*). We are therefore optimistic that the technological requirements for our method to yield a true quantum advantage over classical phase measurements will soon be met.

In this work, the coincidence acquisition speed was limited by the SPAD camera readout scheme and photon detection efficiency (PDE), which resulted in much longer quantum imaging acquisition times than for the classical case. First, we used a SPAD camera intended for general use, which, thus, reads out and transfers information for all pixels regardless of whether they detected a photon or not in every frame. Thus, the shortest achievable frame time is simply the readout time per pixel multiplied by the number of pixels, which in our case is 10.4 µs. This is ~10^3 times longer than the exposure time per frame, leading to a very low duty cycle and correspondingly slow acquisitions. Moreover, as we image with low-photon numbers, a large overhead of useless data (pixels with no detections) is generated. To solve this issue, future work will make use of emerging SPAD arrays specialized for sparse event detection, with optimized asynchronous or event-driven readout schemes that only read out and transfer useful coincidence information (*52*). Second, for a given PDE η, the coincidence detection

efficiency is η^2—in our case, yielding an available coincidence detection rate ~30 times lower than single-photon detection. We anticipate further improvements in detection technology that will allow this problem to be addressed in the foreseeable future. See SM-S8 for more details and a comparison with single-pixel detector scanning-based imaging.

Note that despite also using holographic phase retrieval, the entanglement-enhanced microscope presented in this work is quite different from the quantum-enabled holography technique in (53). In that work, two photons are spatially separated and nonlocal photon correlations are needed for holographic reconstruction. In our system, on the other hand, both entangled photons pass through the sample together, which is the crucial aspect that enables our system to achieve supersensitive phase imaging.

In conclusion, we have successfully implemented a practical large FoV, scan-free quantum-enhanced phase imaging protocol, capable of retrieving phase images with decreased noise compared to equivalent classical measurements. Our system uses space-polarization hyperentanglement, generated by an integrated source of quantum light, and combines a LIM with robust phase-scanning mechanism and several data processing steps of images produced by a SPAD array camera. Polarization entanglement is exploited as a resource for phase supersensitivity, while photon pair spatial correlations ensure that coincidence detections are confined to nearby pixels, thereby enabling scan-free simultaneous multiphoton imaging on many spatial modes across the whole FoV. For birefringent and nonbirefringent phase samples, we measured reductions in noise of the retrieved phase images, by factors of 0.72 ± 0.06 and 0.80 ± 0.04, whose inverse values yield the sensitivity enhancements of 1.39 ± 0.11 and 1.25 ± 0.06, respectively. Precise measurement of a protein microarray demonstrate that biomarkers can be well identified. We expect systematic calibrations of the phase response of specific samples to allow identifying biomarker concentration. This advance shows the compatibility of our quantum-enhanced method with medical diagnostic applications, with further use cases extending to a range of material and biological inspection tasks such as monitoring photoresist-based microfabrication, inspection of semiconductor and crystal materials, and observation of living organisms without inducing cellular damage or photosensitive effects. We believe that, with realistic future developments, our technique will be highly competitive with respect to classical alternatives in which delicate samples cannot be analyzed without risks of being substantially altered or even damaged and that this work is thus an important step toward practically useful quantum imaging.

MATERIALS AND METHODS
Details of experimental setup
As shown in Fig. 1A, a continuous wave single-mode laser (TOPTICA TopMode) at 405.6 nm wavelength is used to pump a type 0 periodically poled potassium titanyl phosphate (ppKTP) crystal inside the SI. A superposition of SPDC processes takes place, which generates the quantum state $|\psi\rangle$, composed of photon pairs at 811.2 nm wavelength (22). The ppKTP crystal is temperature-controlled using a Peltier oven to satisfy the degenerate phase matching condition. The laser power, measured before the SI, was fixed to 3 mW for background measurements and fixed to 0.6 mW for sample measurements. The entangled photon pairs are imaged onto the SLM (HOLOEYE PLUTO-2) using two lenses of focal lengths $L_1 =$

300 mm and $L_2 = 2500$ mm in a 4f configuration and then reimaged with two further lenses ($L_3 = 250$ mm in the measurement of the birefringent sample, $L_3 = 500$ mm in the measurement of the non-birefringent sample, and $L_4 = 500$ mm) again in a 4f configuration into our LIM and SPAD camera (Micro Photon Devices SPC3) (see Fig. 1A). The LIM and camera are separated by less than the Rayleigh range of the imaging system. Therefore, the SLM, the LIM, and the SPAD camera are at conjugate planes of the SPDC plane, where photon pairs are spatially correlated (24). A 810 ± 5 nm band-pass filter (BPF) is placed before the camera to remove environment noise and spurious pump light. Our SPAD camera has a pixel pitch of 150 μm and is fitted with a microlens array, giving an effective pixel fill factor (FF) of ≈75%. Therefore, the overall PDE at 811.2 nm (taking into account FF) is approximately 3%. The SPs (United Crystals) in our LIM induce a shear of 450 μm.

Coincidence counting using a camera
Under low-light conditions, where a pixel receives either zero or one photon, the coincidence counts cc between any two arbitrary pixels i and j can be calculated from N intensity image frames according to (18, 27)

$$cc(i,j) = \sum_{l=1}^{N} I_{l,i} I_{l,j} - \frac{1}{N} \sum_{m,n=1}^{N} I_{m,i} I_{n,j} \qquad (4)$$

where $I_{l,i} \in \{0,1\}$ represents the value returned by the ith pixel in the lth frame. The first term on the right side of Eq. 4 calculates the real and accidental coincidences across all frames, while the second term subtracts the accidentals, leaving only genuine photon coincidences (18). In this work, we calculate three cases for the above formula:

1) $cc_{DD}(i, j)$: Pixels i and j both on the left half of the camera, i.e., a $\langle DD|$ polarization projection;
2) $cc_{AA}(i, j)$: Pixels i and j both on the right half of the camera, i.e., a $\langle AA|$ polarization projection; and
3) $cc_{DA}(i, j)$: Pixels i and j on different halves of the camera, i.e., a $\langle DA|$ polarization projection.

The SPAD camera was operated at a frame rate of 96 kHz, with a dead time of 120 ns. For sample and background measurements, we used an exposure time of 10 and 70 ns per frame, respectively. To collect enough events for accurate statistics and high SNR (as detailed in SM-S5), large numbers of frames were acquired: For the birefringent case, sample and background acquisitions consisted of 2.07×10^9 and 2.76×10^9 frames (6- and 8-hour acquisition times) per PSDH step. For the nonbirefringent case, sample and background acquisitions consisted of 2.42×10^9 and 1.38×10^9 frames (7- and 4-hour acquisition times) per PSDH step.

During acquisitions, frames are first read into the camera's internal memory, which is then emptied via a USB3 link into an external PC random access memory. In parallel, the PC executes a control and analysis script, which calculates Eq. 4 from the incoming frames, and saves the coincidence data to disk.

SPAD array cross-talk removal
Coincidence counts cc_{DD} and cc_{AA}, as calculated by Eq. 4, also include cross-talk. In SPAD cameras, cross-talk coincidences $cc_{ct}(i, j)$ occur because, after a real photon detection in pixel i, photons can be emitted from that location and detected by a nearby pixel j with probability $P_{ct}(j \mid i)$ (54) or vice versa (55). This is modeled by

$$cc_{ct}(i,j) = cc_{ct}(i\,|\,j) + cc_{ct}(j\,|\,i)$$
$$= P_{ct}(i\,|\,j)\sum_{l=1}^{N} I_{l,j} + P_{ct}(j\,|\,i)\sum_{l=1}^{N} I_{l,i} \qquad (5)$$

cc_{DA}, on the other hand, is not affected by cross-talk because, in this case, the monitored pixels are far apart on separate halves of the camera.

Characterizing $P_{ct}(i\,|\,j)$ is a highly nontrivial task, because it requires individual illumination of every single pixel. However, one can approximate the spatially dependent cross-talk to be uniform across the camera, depending only on the distance between two pixels (55, 56)

$$cc_{ct}(i,j) = P_{ct}(\Delta x, \Delta y)\sum_{l=1}^{N}(I_{l,j} + I_{l,i}) \qquad (6)$$

where $\Delta x = |x_i - x_j|$ and $\Delta y = |y_i - y_j|$, with i and j now explicitly expressed in terms of their x and y coordinates.

We characterized $P_{ct}(\Delta x, \Delta y)$ by counting coincidences with the camera sensor covered, such that detections were only generated by dark counts. As dark counts of different pixels are uncorrelated, any coincidences measured are due to cross-talk (57). We then obtain the cross-talk probability

$$P_{ct}(\Delta x, \Delta y) = \frac{1}{I_{tot}}\sum_{i=1}^{M}cc(i, i+\Delta\mathbf{r}) \qquad (7)$$

where $\Delta\mathbf{r} = [\Delta x, \Delta y]$ and $cc(i, i+\Delta\mathbf{r})$ is the coincidence count, calculated using Eq. 4 between the pixels with coordinates $[x_i, y_i]$ and $[x_i + \Delta x, y_i + \Delta y]$. M is the total number of pixel pairs with equal separation $\Delta\mathbf{r}$, and I_{tot} is the total number of detections on all pixels over all frames. See SM-S3 for an image of $P_{ct}(\Delta x, \Delta y)$.

Therefore, the coincidences for the $\langle DD|$ and $\langle AA|$ polarization projections, with cross-talk subtracted, are calculated simply as $cc_{kk}(i,j) \equiv cc(i,j) - cc_{ct}(i,j)$, with $k = \{D, A\}$. This calculation is performed in postprocessing, after an experimental acquisition has completed.

Spatially uncorrelated noise removal

When imaging coincidences, additional sources of noise can appear because of the detection of spatially uncorrelated coincidences. However, these can be removed in postprocessing; as with our experimental apparatus, the probability of genuine coincidence detections becomes negligible for pixel pairs that are well separated. We determine the SPDC photon pairs' spatial correlation width (σ_{fit}), which characterizes the maximum possible distance between correlated photons [see (58)], by fitting the following Gaussian model to the measured coincidence counts

$$G(i,j) = \exp\left[\frac{-\left(\left((x_j - x_{0,i})^2 + (y_j - y_{0,i})^2\right)\right)}{2\,\sigma_{fit}^2}\right] \qquad (8)$$

with $[x_{0,i}, y_{0,i}] = [x_i, y_i]$ for cc_{DD} and cc_{AA}. For cc_{DA}, we have $[x_{0,i}, y_{0,i}] = [x_i + d_x, y_i + d_y]$, where d_x and d_y are additional fitting parameters (details in SM-S3). We then apply the following condition, yielding the filtered coincidence counts cc_F with spatially uncorrelated noise coincidences to be removed

$$cc_F(i,j) = \begin{cases} cc(i,j), & \text{if } G(i,j) > t \\ 0, & \text{otherwise} \end{cases} \qquad (9)$$

where $cc(i,j)$ is calculated as described in the previous section for cc_{DD}, cc_{AA}, and cc_{DA}. t is a threshold between 0 (no filtering) and 1 (filtering out all coincidences). For the phase imaging measurements in this work, a threshold of $t = 0.5$ was used (details in SM-S3).

Phase-shifting interferometry method

PSDH is a well-known technique for quantitative phase retrieval, which requires detecting four intensity images $I(\phi_{Sample}, \alpha)$ with controlled offset phases ($\alpha = \{0, \pi/2, \pi, 3\pi/2\}$ for classical light) to access $\hat{\phi}_{Sample}$ (30). This method originates from an algebraic inversion of the interference dependence function and is usually written as

$$\hat{\phi}_{Sample} = \tan^{-1}\left[\frac{I(\phi_{Sample}, \pi/2) - I(\phi_{Sample}, 3\pi/2)}{I(\phi_{Sample}, \pi) - I(\phi_{Sample}, 0)}\right] \qquad (10)$$

When measuring coincidence images as in our study, the N00N state quantum interference is governed by the phase $2\Theta = 2(\phi_{Sample} + \alpha)$ in Eq. 1, where the factor of 2 represents the superresolution enhancement. Accordingly, the four phase offsets are set to $\{0, \pi/4, \pi/2, 3\pi/4\}$, so that we can retrieve $2\hat{\phi}_{Sample}$, which is therefore divided by 2 to get Eq. 3. To correctly set the four required offset phases, we first scanned through the interference curves by tilting SP_2 (shown in Fig. 2), which produces a continuous scan on α. We then fitted a cosine to the data to extract the right SP_2 tilts for the required offset phases.

Modeling sensitivity enhancement

To model the expected sensitivity enhancement, we compare the noise (standard deviation) of the classical and entanglement-enhanced phase estimates $\hat{\phi}_{Classical}$ and $\hat{\phi}_{N00N}$, calculated using Eqs. 10 and 3, respectively. Using the error propagation formula (59)

$$sd(f) = \sqrt{\sum_j\left[\left(\frac{\partial f}{\partial x_j}\right)^2 sd(x_j)^2\right]} \qquad (11)$$

this noise can be related to the underlying measurements. For classical (N00N) interference, the function f corresponds to $\hat{\phi}_{Classical}$ ($\hat{\phi}_{N00N}$) and x_j to the experimental intensity (coincidence) measurements. The standard deviations $sd(x_j)$ of the intensity and coincidence image measurements, taking into account the real (i.e., imperfect) interference visibility and photon counting noise, can be expressed as

$$sd(I_j) = \begin{cases} \left[\dfrac{\mathcal{V}_{Classical}\cos[\phi_{Sample}(\mathbf{r}) + j\pi/2] + 1}{2} I_{tot}/4\right]^{1/2} & \text{for } I_D \\[3mm] \left[\dfrac{-\mathcal{V}_{Classical}\cos[\phi_{Sample}(\mathbf{r}) + j\pi/2] + 1}{2} I_{tot}/4\right]^{1/2} & \text{for } I_A \end{cases} \qquad (12)$$

where I_D (I_A) is the intensity image measured in the diagonal (antidiagonal) polarization basis (see SM-S5 for details), and

$$sd(ci_j) =$$
$$\begin{cases} \kappa\left[\dfrac{\mathcal{V}\cos[2\phi_{Sample}(\mathbf{r}) + j\pi/4] + 1}{4} ci_{tot}/4\right]^{1/2} & \text{for } cc_{DD} \text{ and } cc_{AA} \\[3mm] \kappa\left[\dfrac{-\mathcal{V}\cos[2\phi_{Sample}(\mathbf{r}) + j\pi/4] + 1}{2} ci_{tot}/4\right]^{1/2} & \text{for } cc_{DA} \end{cases} \qquad (13)$$

Here, I_j (ci_j) is the intensity (coincidence) measurement corresponding to the jth step in the PSDH protocol, and I_{tot} (ci_{tot}) is the total number of photons (coincidences) over all four steps. $\mathcal{V}_{Classical}$

(V) is the interference visibility for classical (N00N) interference, where we set $\mathcal{V}_{Classical}$ to unity, while we measured $\mathcal{V} = 0.94 \pm 0.06$. Some photon counting noise is added by the coincidence counting method used here (*27*, *28*), which is quantified by $\kappa \geq 1$ (where $\kappa = 1$ for ideal shot noise limited measurements). We experimentally measure a value of $\kappa = 1.05$ (see SM-S5 for details).

For a fair sensitivity comparison, we set the total number of photons used in the classical and the entanglement-enhanced phase estimation to be equal, i.e., $I_{tot} = 2c i_{tot}$. Substituting Eqs. 12 and 13 into Eq. 11 gives the standard deviations of the phase estimations retrieved for each polarization measurement for both classical and quantum-enhanced methods. The phase retrievals due to the individual polarization measurements are then combined according to

$$\hat{\phi}_{Classical} = \frac{\hat{\phi}_{Classical,D} + \hat{\phi}_{Classical,A}}{2} \qquad (14)$$

$$\hat{\phi}_{N00N} = \frac{\hat{\phi}_{N00N,DD} + \hat{\phi}_{N00N,AA} + 2\hat{\phi}_{N00N,DA}}{4} \qquad (15)$$

which allows the use of the error propagation formula Eq. 11 again to obtain expressions for both sd($\hat{\phi}_{Classical}$) and sd($\hat{\phi}_{N00N}$) in terms of I_{tot}. Last, we numerically evaluate sd($\hat{\phi}_{N00N}$)/sd($\hat{\phi}_{Classical}$) = 0.79 ± 0.05 (see SM-S5 for details).

Protein microarray sample fabrication

The microarray test sample was fabricated using the commercially available Pierce Recombinant Protein A/G (Thermo Fisher Scientific, 21186). First, the stock solution at 5 mg/ml was diluted using Milli-Q water to a final concentration of 500 µg/ml. This was then spotted (using a SCIENION sciFLEXARRAYER S3 spotter) onto a borosilicate glass slide (NEXTERION Slide E, SCHOTT), coated with a multipurpose epoxysilane layer that covalently binds most types of biomolecules including amino- and nonmodified DNA, RNA, and proteins. Spots of diameter 500 µm were made with 1000-µm center-to-center spacing, and the sample was left to dry overnight (24 hours) before measuring.

SUPPLEMENTARY MATERIALS
Supplementary material for this article is available at https://science.org/doi/10.1126/sciadv.abj2155

REFERENCES AND NOTES

1. V. Giovannetti, S. Lloyd, L. Maccone, Quantum-enhanced measurements: Beating the standard quantum limit. *Science* **306**, 1330–1336 (2004).
2. S. Pirandola, B. R. Bardhan, T. Gehring, C. Weedbrook, S. Lloyd, Advances in photonic quantum sensing. *Nat. Photonics* **12**, 724–733 (2018).
3. D. J. Stephens, V. J. Allan, Light microscopy techniques for live cell imaging. *Science* **300**, 82–86 (2003).
4. R. Lubart, R. Lavi, H. Friedmann, S. Rochkind, Photochemistry and photobiology of light absorption by living cells. *Photomed. Laser Surg.* **24**, 179–185 (2006).
5. K. R. Byrnes, X. Wu, R. W. Waynant, I. K. Ilev, J. J. Anders, Low power laser irradiation alters gene expression of olfactory ensheathing cells in vitro. *Lasers Surg. Med.* **37**, 161–171 (2005).
6. C. A. Casacio, L. S. Madsen, A. Terrasson, M. Waleed, K. Barnscheidt, B. Hage, M. A. Taylor, W. P. Bowen, Quantum-enhanced nonlinear microscopy. *Nature* **594**, 201–206 (2021).
7. N. S. Da Silva, J. W. Potrich, Effect of GaAlAs laser irradiation on enzyme activity. *Photomed. Laser Surg.* **28**, 431–434 (2010).
8. K. Eckert, O. Romero-Isart, M. Rodriguez, M. Lewenstein, E. S. Polzik, A. Sanpera, Quantum non-demolition detection of strongly correlated systems. *Nat. Phys.* **4**, 50–54 (2008).
9. F. Wolfgramm, C. Vitelli, F. A. Beduini, N. Godbout, M. W. Mitchell, Entanglement-enhanced probing of a delicate material system. *Nat. Photonics* **7**, 28–32 (2013).
10. M. W. Mitchell, J. S. Lundeen, A. M. Steinberg, Super-resolving phase measurements with a multiphoton entangled state. *Nature* **429**, 161–164 (2004).
11. T. Nagata, R. Okamoto, J. L. O'Brien, K. Sasaki, S. Takeuchi, Beating the standard quantum limit with four-entangled photons. *Science* **316**, 726–729 (2007).
12. J. P. Dowling, Quantum optical metrology—The lowdown on high-N00N states. *Contemp. Phys.* **49**, 125–143 (2008).
13. V. Giovannetti, S. Lloyd, L. Maccone, Advances in quantum metrology. *Nat. Photonics* **5**, 222–229 (2011).
14. Y. Israel, S. Rosen, Y. Silberberg, Supersensitive polarization microscopy using NOON states of light. *Phys. Rev. Lett.* **112**, 103604 (2014).
15. T. Ono, R. Okamoto, S. Takeuchi, An entanglement-enhanced microscope. *Nat. Commun.* **4**, 2426 (2013).
16. D. Gabor, A new microscopic principle. *Nature* **161**, 777–778 (1948).
17. P.-A. Moreau, E. Toninelli, T. Gregory, M. J. Padgett, Imaging with quantum states of light. *Nat. Rev. Phys.* **1**, 367–380 (2019).
18. H. Defienne, M. Reichert, J. W. Fleischer, General model of photon-pair detection with an image sensor. *Phys. Rev. Lett.* **120**, 203604 (2018).
19. D. Bronzi, F. Villa, S. Tisa, A. Tosi, F. Zappa, D. Durini, S. Weyers, W. Brockherde, 100 000 Frames/s 64 × 32 single-photon detector array for 2-D imaging and 3-D ranging. *IEEE J. Sel. Top. Quantum Electron.* **20**, 354–363 (2014).
20. L. Sawyer, D. T. Grubb, G. F. Meyers, *Polymer Microscopy* (Springer, ed. 3, 2008).
21. R. A. Terborg, J. Pello, I. Mannelli, J. P. Torres, V. Pruneri, Ultrasensitive interferometric on-chip microscopy of transparent objects. *Sci. Adv.* **2**, e1600077 (2016).
22. F. Steinlechner, M. Gilaberte, M. Jofre, T. Scheidl, J. P. Torres, V. Pruneri, R. Ursin, Efficient heralding of polarization-entangled photons from type-0 and type-II spontaneous parametric downconversion in periodically poled KTiOPO$_4$. *JOSA B* **31**, 2068–2076 (2014).
23. D. S. Tasca, S. P. Walborn, P. H. Souto Ribeiro, F. Toscano, P. Pellat-Finet, Propagation of transverse intensity correlations of a two-photon state. *Phys. Rev. A* **79**, 033801 (2009).
24. H. Di Lorenzo Pires, M. P. van Exter, Near-field correlations in the two-photon field. *Phys. Rev. A* **80**, 053820 (2009).
25. F. Yesilkoy, R. A. Terborg, J. Pello, A. A. Belushkin, Y. Jahani, V. Pruneri, H. Altug, Phase-sensitive plasmonic biosensor using a portable and large field-of-view interferometric microarray imager. *Light* **7**, 17152 (2018).
26. C. Zhang, J. Zhao, Y. Sun, Influences of the thickness, misalignment, and dispersion of the Savart polariscope on the optical path difference and spectral resolution in the polarization interference imaging spectrometer. *Appl. Opt.* **50**, 3497–3504 (2011).
27. B. Ndagano, H. Defienne, A. Lyons, I. Starshynov, F. Villa, S. Tisa, D. Faccio, Imaging and certifying high-dimensional entanglement with a single-photon avalanche diode camera. *Npj Quantum Inf.* **6**, 94 (2020).
28. M. Reichert, H. Defienne, J. W. Fleischer, Optimizing the signal-to-noise ratio of biphoton distribution measurements. *Phys. Rev. A* **98**, 013841 (2018).
29. S. Slussarenko, M. M. Weston, H. M. Chrzanowski, L. K. Shalm, V. B. Verma, S. W. Nam, G. J. Pryde, Unconditional violation of the shot-noise limit in photonic quantum metrology. *Nat. Photonics* **11**, 700–703 (2017).
30. D. Malacara, *Optical Shop Testing* (Wiley, ed. 3, 2007).
31. R. L. Stears, T. Martinsky, M. Schena, Trends in microarray analysis. *Nat. Med.* **9**, 140–145 (2003).
32. J. Icha, M. Weber, J. C. Waters, C. Norden, Phototoxicity in live fluorescence microscopy, and how to avoid it. *BioEssays* **39**, 1700003 (2017).
33. M. A. Taylor, W. P. Bowen, Quantum metrology and its application in biology. *Phys. Rep.* **615**, 1–59 (2016).
34. Y. Park, C. Depeursinge, G. Popescu, Quantitative phase imaging in biomedicine. *Nat. Photonics* **12**, 578–589 (2018).
35. P. Dey, N. Fabri-Faja, O. Calvo-Lozano, R. A. Terborg, A. Belushkin, F. Yesilkoy, A. Fàbrega, J. C. Ruiz-Rodriguez, R. Ferrer, J. J. González-López, M. C. Estévez, H. Altug, V. Pruneri, L. M. Lechuga, Label-free bacteria quantification in blood plasma by a bioprinted microarray based interferometric point-of-care device. *ACS Sens.* **4**, 52–60 (2019).
36. S. P. Hui, T. C. Nag, S. Ghosh, Characterization of proliferating neural progenitors after spinal cord injury in adult zebrafish. *PLOS ONE* **10**, e0143595 (2015).
37. I. Afek, O. Ambar, Y. Silberberg, High-NOON states by mixing quantum and classical light. *Science* **328**, 879–881 (2010).
38. G. Rainò, M. A. Becker, M. I. Bodnarchuk, R. F. Mahrt, M. V. Kovalenko, T. Stöferle, Superfluorescence from lead halide perovskite quantum dot superlattices. *Nature* **563**, 671–675 (2018).
39. G. Peniakov, Z.-E. Su, A. Beck, D. Cogan, O. Amar, D. Gershoni, Towards supersensitive optical phase measurement using a deterministic source of entangled multiphoton states. *Phys. Rev. B* **101**, 245406 (2020).
40. Y. Maleki, A. M. Zheltikov, A high-N00N output of harmonically driven cavity QED. *Sci. Rep.* **9**, 16780 (2019).
41. K. Morimoto, A. Ardelean, M.-L. Wu, A. C. Ulku, I. M. Antolovic, C. Bruschini, E. Charbon, Megapixel time-gated SPAD image sensor for 2D and 3D imaging applications. *Optica* **7**, 346–354 (2020).

42. N. Thomas-Peter, B. J. Smith, A. Datta, L. Zhang, U. Dorner, I. A. Walmsley, Real-world quantum sensors: Evaluating resources for precision measurement. *Phys. Rev. Lett.* **107**, 113603 (2011).

43. M. Sanzaro, P. Gattari, F. Villa, A. Tosi, G. Croce, F. Zappa, Single-photon avalanche diodes in a 0.16 μm BCD technology with sharp timing response and red-enhanced sensitivity. *IEEE J. Sel. Top. Quantum Electron.* **24**, 3801209 (2018).

44. D. V. Reddy, D. V. Reddy, R. R. Nerem, S. W. Nam, R. P. Mirin, V. B. Verma, Superconducting nanowire single-photon detectors with 98% system detection efficiency at 1550 nm. *Optica* **7**, 1649–1653 (2020).

45. Q.-Y. Zhao, D. Zhu, N. Calandri, A. E. Dane, A. N. McCaughan, F. Bellei, H.-Z. Wang, D. F. Santavicca, K. K. Berggren, Single-photon imager based on a superconducting nanowire delay line. *Nat. Photonics* **11**, 247–251 (2017).

46. E. E. Wollman, E. E. Wollman, V. B. Verma, V. B. Verma, A. E. Lita, W. H. Farr, M. D. Shaw, R. P. Mirin, S. W. Nam, Kilopixel array of superconducting nanowire single-photon detectors. *Opt. Express* **27**, 35279–35289 (2019).

47. B. L. Higgins, D. W. Berry, S. D. Bartlett, H. M. Wiseman, G. J. Pryde, Entanglement-free Heisenberg-limited phase estimation. *Nature* **450**, 393–396 (2007).

48. G. S. Thekkadath, M. E. Mycroft, B. A. Bell, C. G. Wade, A. Eckstein, D. S. Phillips, R. B. Patel, A. Buraczewski, A. E. Lita, T. Gerrits, S. W. Nam, M. Stobińska, A. I. Lvovsky, I. A. Walmsley, Quantum-enhanced interferometry with large heralded photon-number states. *Npj Quantum Inf.* **6**, 89 (2020).

49. M. Kacprowicz, R. Demkowicz-Dobrzański, W. Wasilewski, K. Banaszek, I. Walmsley, Experimental quantum-enhanced estimation of a lossy phase shift. *Nat. Photonics* **4**, 357–360 (2010).

50. D. Braun, G. Adesso, F. Benatti, R. Floreanini, U. Marzolino, M. W. Mitchell, S. Pirandola, Quantum-enhanced measurements without entanglement. *Rev. Mod. Phys.* **90**, 035006 (2018).

51. S.-W. Lee, S.-Y. Lee, J. Kim, Optimal quantum phase estimation with generalized multi-component Schrödinger cat states. *JOSA B* **37**, 2423–2429 (2020).

52. F. Madonini, F. Severini, F. Zappa, F. Villa, Single photon avalanche diode arrays for quantum imaging and microscopy. *Adv. Quantum Technol.* **4**, 2100005 (2021).

53. H. Defienne, B. Ndagano, A. Lyons, D. Faccio, Polarization entanglement-enabled quantum holography. *Nat. Phys.* **17**, 591–597 (2021).

54. I. Rech, A. Ingargiola, R. Spinelli, I. Labanca, S. Marangoni, M. Ghioni, S. Cova, Optical crosstalk in single photon avalanche diode arrays: A new complete model. *Opt. Express* **16**, 8381–8394 (2008).

55. B. Eckmann, B. Bessire, M. Unternährer, L. Gasparini, M. Perenzoni, A. Stefanov, Characterization of space-momentum entangled photons with a time resolving CMOS SPAD array. *Opt. Express* **28**, 31553–31571 (2020).

56. G. Lubin, R. Tenne, I. Michel Antolovic, E. Charbon, C. Bruschini, D. Oron, Quantum correlation measurement with single photon avalanche diode arrays. *Opt. Express* **27**, 32863–32882 (2019).

57. A. Ficorella, L. Pancheri, G.-F. D. Betta, P. Brogi, G. Collazuol, P. S. Marrocchesi, F. Morsani, L. Ratti, A. Savoy-Navarro, Crosstalk mapping in CMOS SPAD arrays, in *2016 46th European Solid-State Device Research Conference (ESSDERC)* (Lausanne, Switzerland. 2016), pp. 101–104.

58. H. Defienne, M. Reichert, J. W. Fleischer, D. Faccio, Quantum image distillation. *Sci. Adv.* **5**, eaax0307 (2019).

59. H. H. Ku, Notes on the use of propagation of error formulas. *J. Res. Natl. Bur. Stand.* **70C**, 263–273 (1966).

60. L. M. Procopio, O. Rosas-Ortiz, V. Velázquez, On the geometry of spatial biphoton correlation in spontaneous parametric down conversion. *Math. Methods Appl. Sci.* **38**, 2053–2061 (2015).

61. C. I. Osorio, A. Valencia, J. P. Torres, Spatiotemporal correlations in entangled photons generated by spontaneous parametric down conversion. *New J. Phys.* **10**, 113012 (2008).

62. M. P. Edgar, D. S. Tasca, F. Izdebski, R. E. Warburton, J. Leach, M. Agnew, G. S. Buller, R. W. Boyd, M. J. Padgett, Imaging high-dimensional spatial entanglement with a camera. *Nat. Commun.* **3**, 984 (2012).

63. M. Tsang, Quantum imaging beyond the diffraction limit by optical centroid measurements. *Phys. Rev. Lett.* **102**, 253601 (2009).

64. M. Avendaño-Alejo, M. Rosete-Aguilar, Optical path difference in a plane-parallel uniaxial plate. *JOSA A* **23**, 926–932 (2006).

65. L. Di Stefano, S. Mattoccia, F. Tombari, ZNCC-based template matching using bounded partial correlation. *Pattern Recogn. Lett.* **26**, 2129–2134 (2005).

66. M. P. Edgar, G. M. Gibson, M. J. Padgett, Principles and prospects for single-pixel imaging. *Nat. Photonics* **13**, 13–20 (2019).

67. F. Madonini, F. Severini, A. Incoronato, E. Conca, F. Villa, Design of a 24× 24 SPAD imager for multi-photon coincidence-detection in super resolution microscopy. *Quantum Opt. Photon Counting* **11771**, 117710B (2021).

68. M. V. Jabir, G. K. Samanta, Robust, high brightness, degenerate entangled photon source at room temperature. *Sci. Rep.* **7**, 12613 (2017).

69. J. Arlt, D. Tyndall, B. R. Rae, D. D.-U. Li, J. A. Richardson, R. K. Henderson, A study of pile-up in integrated time-correlated single photon counting systems. *Rev. Sci. Instrum.* **84**, 103105 (2013).